

The Inclusive Two Jet Triply Differential Cross Section

W. T. Giele

*Fermi National Accelerator Laboratory, P. O. Box 500,
Batavia, IL 60510, U.S.A.*

E. W. N. Glover

*Physics Department, University of Durham,
Durham DH1 3LE, England*

and

David A. Kosower

*Service de Physique Théorique, Centre d'Etudes de Saclay,
F-91191 Gif-sur-Yvette cedex, France*

November 7 1994

Abstract

We study the inclusive two jet triply differential cross section $d^3\sigma/dE_T d\eta_1 d\eta_2$ at Fermilab energies. Different η_1 and η_2 pseudorapidity regions are directly related to both the parton level matrix elements and the parton densities at leading order. We present the next-to-leading order [$\mathcal{O}(\alpha_s^3)$] corrections and show that the shape of the distribution at fixed transverse energy E_T is a particularly powerful tool for constraining the parton distributions at small to moderate x values. We investigate the renormalisation/factorisation scale uncertainty present in the normalisation and shape of the distribution at next-to-leading order. We discuss specific slices of the distribution, the same-side/opposite side ratio and the signed pseudorapidity distribution, in detail and compare them with preliminary experimental data.

1 Introduction

Dijet production in hadron collisions occurs when two partons from the incident hadrons undergo a hard pointlike interaction and scatter at relatively large angles. The two-jet cross section depends on both the non-perturbative probability of finding a particular parton inside the parent hadron and the dynamics of the hard scattering. By examining kinematic regions where the parton densities are well known, we can probe the pointlike strong-interaction cross section. One example of this is the shape of the angular distribution of the jets in their centre of mass frame. Recent data provide clear evidence that a running coupling constant, as given by QCD, is needed to describe the data [1] and that the next-to-leading order QCD predictions [2] are in good agreement with the data. An alternative approach is to use the theoretical description of the hard scattering to extract the distribution of partons in the proton from the data. This is particularly interesting since gluon scattering plays a very important role in two jet production, and it may be possible to probe the gluon density in a more direct way than is possible in deeply inelastic scattering or in Drell-Yan processes.

The inclusive two-jet cross section can be described in terms of variables most suited to the geometry of the detector; the transverse energy of the leading jet, $E_T = E_{T1}$, and the pseudorapidities of the two leading jets, η_1 and η_2 . Recently, the D0 collaboration has presented a preliminary measurement of $d^3\sigma/dE_T d\eta_1 d\eta_2$ [1] as a function of η_1 and η_2 at fixed E_T . This seemingly complicated three-dimensional quantity contains all the information available from two jet events. In particular, at leading order, η_1 and η_2 are directly related to the parton momentum fractions x_1, x_2 ,

$$\begin{aligned}x_1 &= \frac{E_T}{\sqrt{s}} (\exp(\eta_1) + \exp(\eta_2)), \\x_2 &= \frac{E_T}{\sqrt{s}} (\exp(-\eta_1) + \exp(-\eta_2)),\end{aligned}\tag{1}$$

so that a measurement of the triply differential cross section $d^3\sigma/dE_T d\eta_1 d\eta_2$ at fixed E_T corresponds to a measurement of $d^2\sigma/dx_1 dx_2$. Although the overall normalisation of cross sections is uncertain in perturbative QCD, one might hope that the shape of this distribution is well-predicted and that it can be used to discriminate between different parton densities. Inclusion of the next-to-leading order corrections enhances the reliability of the calculation for both shape and normalisation.

Beyond leading order, however, Eq. 1 is no longer satisfied and the parton momentum fractions are only approximately determined by the transverse energies and pseudorapidities of the jets. A three-dimensional plot may obscure some of the desired physics, so both the CDF [3] and D0 [1, 4] collaborations have focused on particular slices of the general distribution. The CDF collaboration has examined the ratio of cross sections for same-side events ($\eta_1 \sim \eta_2$) to opposite-side events ($\eta_1 \sim -\eta_2$) for different E_T bins. This reduces the normalization uncertainty and enhances the small x region, $x \sim 4E_T^2/s$. At small transverse

energies, this distribution can reliably discriminate between singular ($xg(x) \sim x^{-0.5}$ at small x) and non-singular $xg(x) \sim x^0$ behavior of the gluon distribution [5]. The D0 collaboration has taken slices in η_1 which contain information over the whole x range, $4E_T^2/s < x < 1$, but are more sensitive to the overall normalisation. In this paper, we study the shape of the distribution over the whole η_1 - η_2 plane. First, we examine the triply-differential distribution at lowest order. We discuss how the available phase space grows as the number of final state partons increases and relate different η_1 and η_2 regions to both the parton level matrix elements and the parton densities (section 2). The full next-to-leading order triply-differential cross section is presented in section 3. We show that it is sensitive to the parton density functions and indicate how the shape depends on the renormalisation (and factorisation) scale. Our results are applied to the CDF same-side/opposite-side and D0 signed distributions in sections 4 and 5. Finally, our main findings are summarised in section 6.

2 The $\mathcal{O}(\alpha_s^2)$ triply differential two jet cross section

The lowest order cross section is given by,

$$\frac{d^3\sigma}{dE_T d\eta_1 d\eta_2} = \frac{1}{8\pi} \sum_{ij} x_1 f_i(x_1, \mu_F) x_2 f_j(x_2, \mu_F) \frac{\alpha_s^2(\mu_R)}{E_T^3} \frac{|\mathcal{M}_{ij}(\eta^*)|^2}{\cosh^4 \eta^*}, \quad (2)$$

where $f_i(x, \mu_F)$ ($i = g, q, \bar{q}$) represents the density of parton i in the proton at factorisation scale μ_F and $|\mathcal{M}_{ij}|^2$ is the lowest order squared matrix element for $ij \rightarrow 2$ partons summed and averaged over initial and final state spins and colours. The strong coupling constant α_s is evaluated at the renormalisation scale, μ_R . The parton level cross section is insensitive to Lorentz boosts and $|\mathcal{M}_{ij}|^2$ therefore depends only on the parton pseudorapidity in the parton-parton rest frame, $\eta^* = (\eta_1 - \eta_2)/2$. To understand how the cross section is distributed over the $\eta_1 - \eta_2$ plane, we recall the ‘single effective subprocess approximation’ [6]. In this approximation all parton-parton scattering cross sections are taken to be equal but are weighted by colour arguments. Thus the gluon-gluon, quark-gluon and quark-quark subprocesses are in the ratio $1 : \frac{4}{9} : \left(\frac{4}{9}\right)^2$ so that,

$$\frac{d^3\sigma}{dE_T d\eta_1 d\eta_2} \sim \frac{1}{8\pi} x_1 F(x_1, \mu) x_2 F(x_2, \mu) \frac{\alpha_s^2(\mu)}{E_T^3} \frac{|\mathcal{M}_{gg}(\eta^*)|^2}{\cosh^4 \eta^*}, \quad (3)$$

where $F(x, \mu)$ is the ‘single effective parton density’,

$$F(x, \mu) = g(x, \mu) + \frac{4}{9} \sum_q (q(x, \mu) + \bar{q}(x, \mu)). \quad (4)$$

A rough indication of how the physical cross section depends on η_1 and η_2 can be obtained by studying the parton-parton luminosity, $x_1 F(x_1, \mu) x_2 F(x_2, \mu)$, and the squared matrix elements, $|\mathcal{M}_{gg}|^2 / \cosh^4 \eta^*$, for gluon-gluon scattering separately.

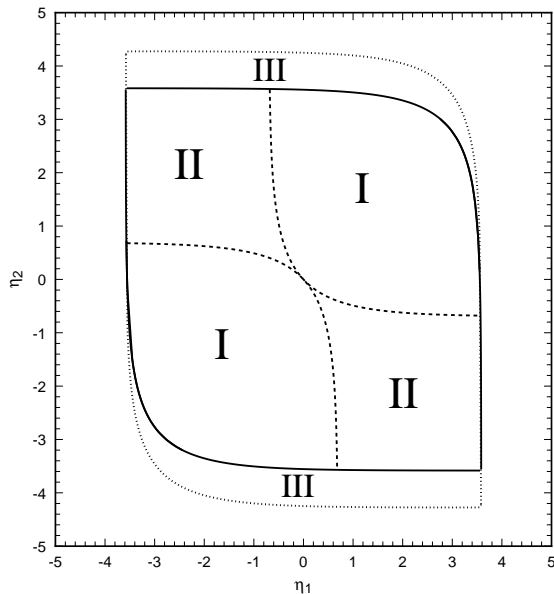


Figure 1: The phase space boundary in the $\eta_1 - \eta_2$ plane at leading-order (solid) and next-to-leading order (dotted) for $E_T = 50$ GeV and $\sqrt{s} = 1800$ GeV. The dashed line separates the ‘small’ x – ‘large’ x and ‘large’ x – ‘large’ x regions. In region I, either x_1 or x_2 is less than x_T , while in region II, both x_1 and x_2 are bigger than x_T . Region III is only permitted at next-to-leading order.

However, to orient ourselves in the $\eta_1 - \eta_2$ plane, we first focus on the allowed phase space in terms of η_1 and η_2 . At lowest order, the jet pseudorapidities are directly related to the parton fractions via Eq. 1. Since the momentum fraction cannot exceed unity, we find,

$$-\log\left(\frac{2 - x_T \exp(-\eta_1)}{x_T}\right) < \eta_2 < \log\left(\frac{2 - x_T \exp(\eta_1)}{x_T}\right), \quad (5)$$

and,

$$|\eta_1| < \cosh^{-1}\left(\frac{1}{x_T}\right), \quad (6)$$

where $x_T = 2E_T/\sqrt{s}$ and $x_T^2 < x_1 x_2 < 1$. This boundary is shown in Fig. 1 for $E_T = 50$ GeV and $\sqrt{s} = 1800$ GeV. For the opposite-side cross section, $\eta_1 \sim -\eta_2$, the parton fractions are roughly equal so that in the top left and bottom right corners of the allowed phase space, $x_1 \sim x_2 \rightarrow 1$. On the other hand, in the bottom left and top right corners, corresponding to same-side events with $\eta_1 \sim \eta_2$, the parton fractions are maximally different, $x_1 \rightarrow x_T^2$, $x_2 \rightarrow 1$ and vice versa. The dashed boundary separating region I and II makes a nominal division of the phase space according to whether both parton fractions are ‘large’ or one parton fraction is ‘small’. In region II, x_1 and $x_2 > x_T$ while in region I, either $x_1 < x_T$ or $x_2 < x_T$. The corresponding axes for the pseudorapidities of the two jet system in the laboratory, $\eta_{\text{boost}} = (\eta_1 + \eta_2)/2$, and of the jet in the jet-jet center of mass frame, $\eta^* = (\eta_1 - \eta_2)/2$, are related by a rotation of 45° .

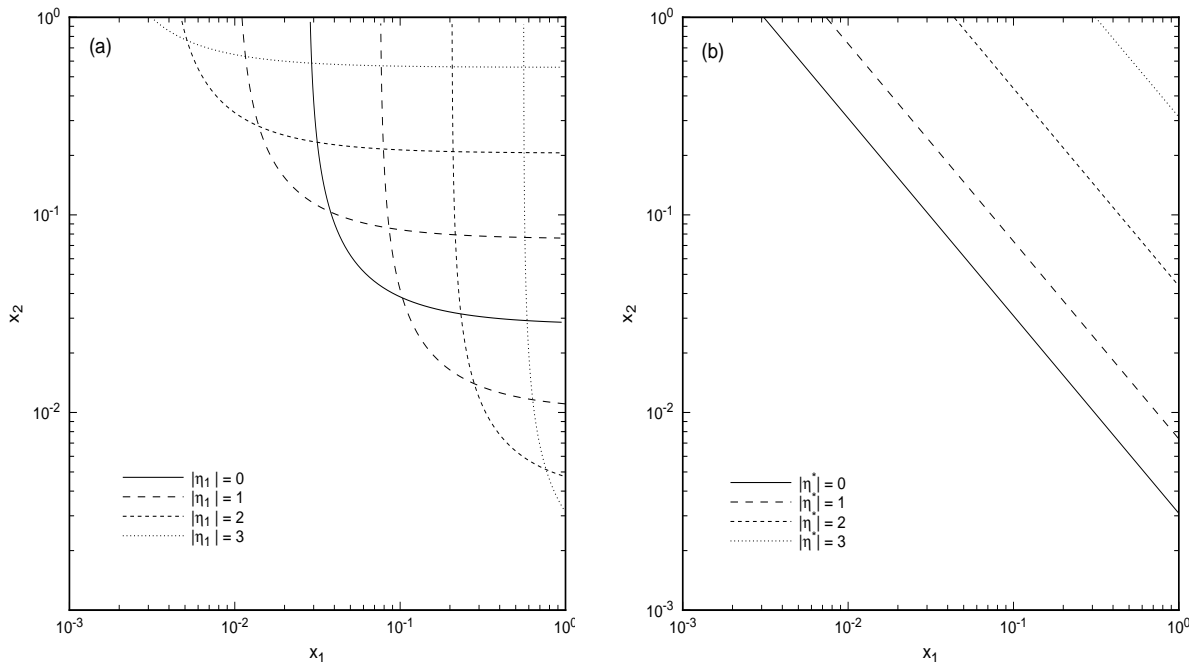


Figure 2: Contours of (a) constant η_1 and (b) constant η^* in the $x_1 - x_2$ plane for $E_T = 50$ GeV and $\sqrt{s} = 1800$ GeV.

At lowest order in perturbative QCD, each point in the $\eta_1 - \eta_2$ plane is uniquely related to the parton momentum fractions x_1 and x_2 via Eq. 1. To give an idea of how different x values are spread over the allowed pseudorapidities, we show contours of fixed η_1 in the $x_1 - x_2$ plane in Fig. 2. At fixed η_1 , the smallest x_1 value occurs when η_2 is a minimum, while η_2 is a maximum for the smallest x_2 value. An alternative way of looking at the $x_1 - x_2$ plane using the η^* and η_{boost} variables is shown in Fig. 2b. For a given η^* , varying η_{boost} over its allowed range takes $(x_1, x_2) = (1, x_T^2 \cosh^2(\eta^*))$ to $(x_1, x_2) = (x_T^2 \cosh^2(\eta^*), 1)$ while preserving $x_1 x_2 = x_T^2 \cosh^2(\eta^*)$. These contours are particularly useful since the parton matrix elements depend only on η^* and not on η_{boost} .

Although the charged parton distributions have been probed directly over a wide range of parton momentum fractions x and scales Q^2 in deeply inelastic scattering, the gluon density is rather poorly known. Direct photon data from WA70 [7] determine the shape of the gluon in the $x \sim 0.3 - 0.4$ region, however, the gluon density at other x values is only constrained by the momentum sum rule. To explore the sensitivity of the triply differential cross section, we choose parton density functions with contrasting small- x behaviours; the improved MRSD₋ and MRSD₀ distributions of ref. [8] for which $xg(x)$ behave as $x^{-0.5}$ and x^0 respectively at small x and Q^2 . The low- x behaviour of F_2^{ep} measured at HERA is better fitted by an $x^{-0.3}$ growth as parameterised by the MRSA distributions [9], however the range of predictions from the MRSD₋ and MRSD₀ distributions indicate where the triply differential cross section is sensitive to the small- x parton distributions. It is worth noting that because of the momentum sum rule, a parton density that is relatively large at $x \sim 10^{-3}$ must be relatively small at $x \sim \text{few} \times 10^{-2}$. This is demonstrated in Fig. 3a where we show the ratio of the ‘single effective parton density’ for the MRSD₀ and MRSD₋ parton density

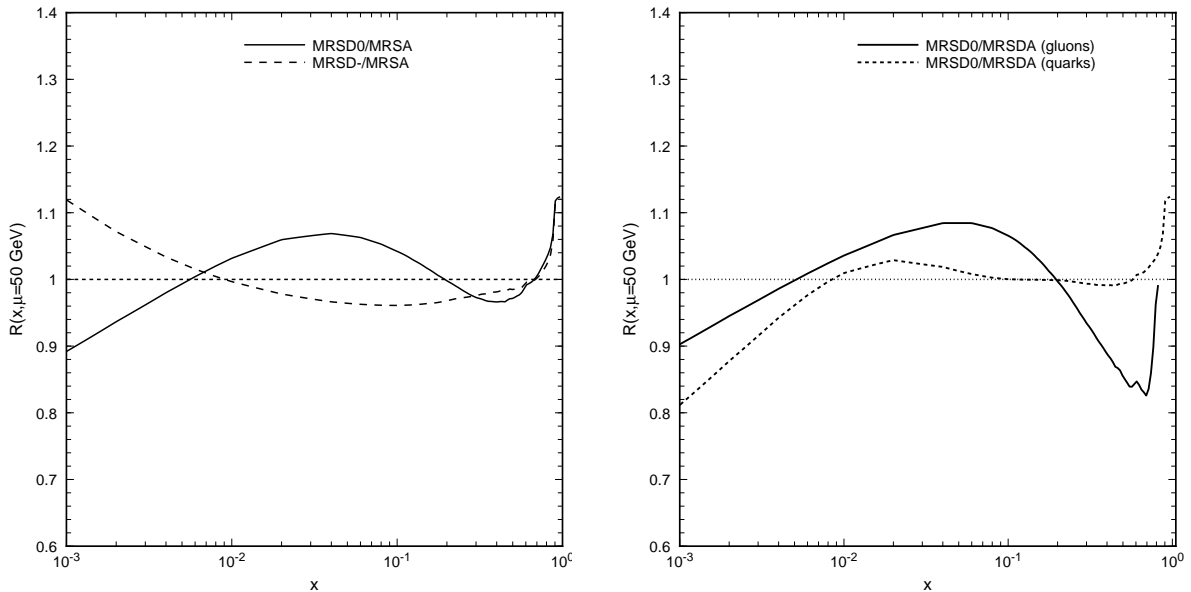


Figure 3: (a) The ratio of the ‘single effective parton density’ of Eq. 4 for the MRSD₀ and MRSD₋ distributions compared to the MRSA parameterisation at $\mu = 50$ GeV. (b) The ratio of the gluon and quark parton densities in the MRSD₀ distribution compared to the MRSA parameterisation at the same scale.

functions relative to that of the MRSA parameterisation. The hierarchy evident at small x is reversed in the moderate x range, where the MRSD₀ density is 15% larger than that for the MRSD₋ density functions.

At $x \sim 1$, the MRSD distributions are both larger than MRSA. This is primarily because the up and down valence distributions are fitted separately in the more recent MRS parameterisations rather than the up and the (up plus down) valence combination. In any event, the distribution of partons inside the proton with $x > 0.5$ is very small and poorly constrained by data.

If we examine the gluon and the quark densities separately (the latter summed over all quark and anti-quark flavors), shown in Fig. 3b, then we find that other than at small x , the quark densities are quite well determined by present-day data: different sets are quite similar. In contrast, it is the gluon densities that are poorly determined: different sets are substantially different even at intermediate x . As suggested by the ‘single effective parton density,’ and as we shall see in greater detail, the gluon densities are sufficiently important to jet production in hadron-hadron scattering to cause substantial variations in predictions dependent on the densities at moderate x .

As can be seen from Eq. 2, the cross section is proportional to the product of structure functions. To get a feeling for how this product varies, Fig. 4 shows the parton-parton luminosity in the single effective subprocess approximation as a function of η_{boost} for different

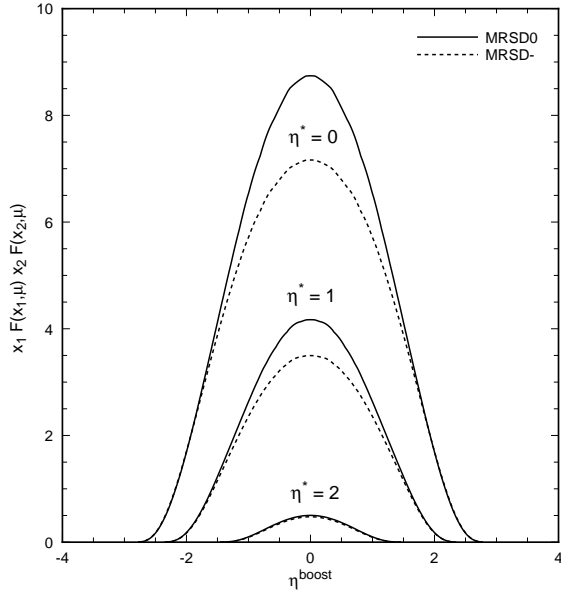


Figure 4: The parton-parton luminosity for the MRSD₀ and MRSD₋ parton densities in the ‘single effective subprocess approximation’ as a function of η_{boost} for $|\eta^*| = 0, 1$ and 2 and $\mu = 50$ GeV.

$|\eta^*|$ values. This corresponds to diagonal strips across the $\eta_1 - \eta_2$ plane. As expected, the largest luminosity occurs when x_1 and x_2 are equally small, $\eta^* \sim \eta_{\text{boost}} = 0$. Once again, the MRSD₀ luminosity is approximately 20% larger than that for MRSD₋. As either $|\eta_{\text{boost}}|$ or $|\eta^*|$ increases, the luminosity decreases rapidly. However the falloff is more rapid with increasing $|\eta^*|$ than with increasing $|\eta_{\text{boost}}|$.

As mentioned earlier, the parton-parton subprocess scattering matrix elements are independent of η_{boost} . One consequence is that for fixed η^* , the only variation of the cross section comes from the variation of the parton densities as η_{boost} runs over the allowed kinematic range. The lowest order squared matrix elements for $gg \rightarrow gg$ scattering are given by,

$$\frac{|\mathcal{M}_{gg}|^2}{\cosh^4(\eta^*)} = \frac{9\pi^2 (4 \cosh^2(\eta^*) - 1)^3}{8 \cosh^6(\eta^*)}. \quad (7)$$

These matrix elements are plotted in Fig. 5 as a function of η^* . At small $|\eta^*|$ the matrix elements grow rapidly until $|\eta^*| \sim 2$ where the matrix elements saturate. This behaviour complements the parton-parton luminosity which is largest at $\eta^* = 0$.

By multiplying the parton-parton luminosity with the squared matrix elements (along with the overall factor $\alpha_s^2(\mu)/8\pi E_T^3$) we obtain the physical cross section. Because different parton distributions dominate for different momentum fractions (and hence η_1 and η_2 values), we expect the shape of the triply-differential cross section to be sensitive to the parton densities. This is illustrated in Fig. 6, where we show the leading order prediction for the

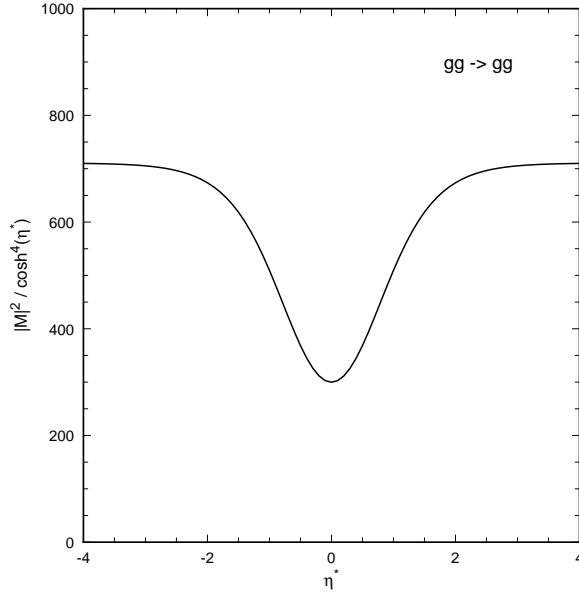


Figure 5: The lowest order squared matrix elements $|\mathcal{M}_{gg}|^2 / \cosh^4(\eta^*)$ for $gg \rightarrow gg$ scattering as a function of η^* .

ratio,

$$R = \frac{\int_{E_{T\min}}^{E_{T\max}} dE_T \left(\frac{d^3\sigma}{dE_T d\eta_1 d\eta_2}(\text{MRSD}_0) - \frac{d^3\sigma}{dE_T d\eta_1 d\eta_2}(\text{MRSD}_-) \right)}{\int_{E_{T\min}}^{E_{T\max}} dE_T \frac{d^3\sigma}{dE_T d\eta_1 d\eta_2}(\text{MRSD}_-)}, \quad (8)$$

in the transverse energy range $45 \text{ GeV} < E_T < 55 \text{ GeV}$ evaluated at $\mu = E_T^1$. In addition to the sharp cutoff marking the boundary of the allowed phase space, the excess of MRSD_0 over MRSD_- at small η_1 and η_2 and the depletion at large $|\eta_1| \sim |\eta_2|$ are seen clearly. Over the whole $\eta_1 - \eta_2$ plane, the relative cross sections vary by +23% to -5%, with the most sizeable effects at $\eta_1 \sim \eta_2 \sim 0$ where the cross section is largest. At lowest order, $E_{T1} = E_{T2} = E_T$, so that the distribution is symmetric under $\eta_1 \leftrightarrow \eta_2$.

3 The $\mathcal{O}(\alpha_s^3)$ triply differential two jet cross section

At next-to-leading order, some contributions admit three partons into the final state; for these, the parton fractions are given by,

$$x_{1,2} = \frac{E_{T1}}{\sqrt{s}} \left(\exp(\pm\eta_1) + \frac{E_{T2}}{E_{T1}} \exp(\pm\eta_2) + \frac{E_{T3}}{E_{T1}} \exp(\pm\eta_3) \right), \quad (9)$$

where E_{Ti} and η_i ($i = 1, \dots, 3$) describe the transverse energies and pseudorapidities of the three partons ordered in decreasing E_T . Since the transverse energies of the partons are no

¹The raw cross sections are histogrammed in 0.5×0.5 bins in η_1 and η_2 .

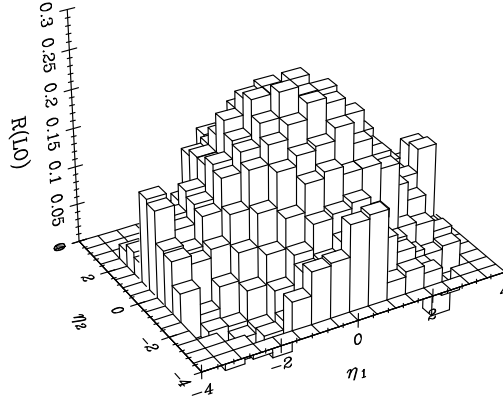


Figure 6: The leading order prediction for the ratio of the triply differential cross section $R(LO)$ defined in Eq. 8 for $45 \text{ GeV} < E_T < 55 \text{ GeV}$ and $\mu = E_T$.

longer forced to be equal, $|\eta_2|$ may increase to compensate for having a smaller transverse energy, $E_{T2}/E_{T1} < 1$. The maximum possible values of $|\eta_2|$ occur when $E_{T2} = E_{T3}$,

$$-\log\left(\frac{a\bar{a} + \sqrt{a^2\bar{a}^2 - a\bar{a}}}{a}\right) < \eta_2 < \log\left(\frac{a\bar{a} + \sqrt{a^2\bar{a}^2 - a\bar{a}}}{\bar{a}}\right), \quad (10)$$

where $a = (2 - x_{T1} \exp(\eta_1))/x_{T1}$ and $\bar{a} = (2 - x_{T1} \exp(-\eta_1))/x_{T1}$. The enlargement of phase space is shown in Fig. 1 (region III). We see that the maximum allowed value of $|\eta_1|$ is unchanged at next-to-leading order so that the physical cross section will exhibit a rather sharp cutoff as $|\eta_1|$ increases. On the other hand there will be a more gradual fall off in the cross section as $|\eta_2|$ increases. Indeed, adding more partons into the final state further increases the allowed η_2 range corresponding to the production of more and more soft partons.

To compute the next-to-leading order cross section, we use an $\mathcal{O}(\alpha_s^3)$ Monte Carlo program for one, two and three jet production based on the one-loop $2 \rightarrow 2$ and the tree level $2 \rightarrow 3$ parton scattering amplitudes [10, 11] described in ref. [12]. This program uses the techniques of refs. [13, 14] to cancel the infrared and ultraviolet singularities thereby rendering the $2 \rightarrow 2$ and $2 \rightarrow 3$ parton processes finite and amenable to numerical computation. The parton four momenta are then passed through a jet algorithm to determine the one, two and three jet cross sections according to the experimental cuts. Different cuts and/or jet algorithms can easily be applied to the parton four-momenta and, in principle, any infrared-safe distribution can be computed at $\mathcal{O}(\alpha_s^3)$.

In order to compare the theory with experiment, we use the parton level equivalent of the

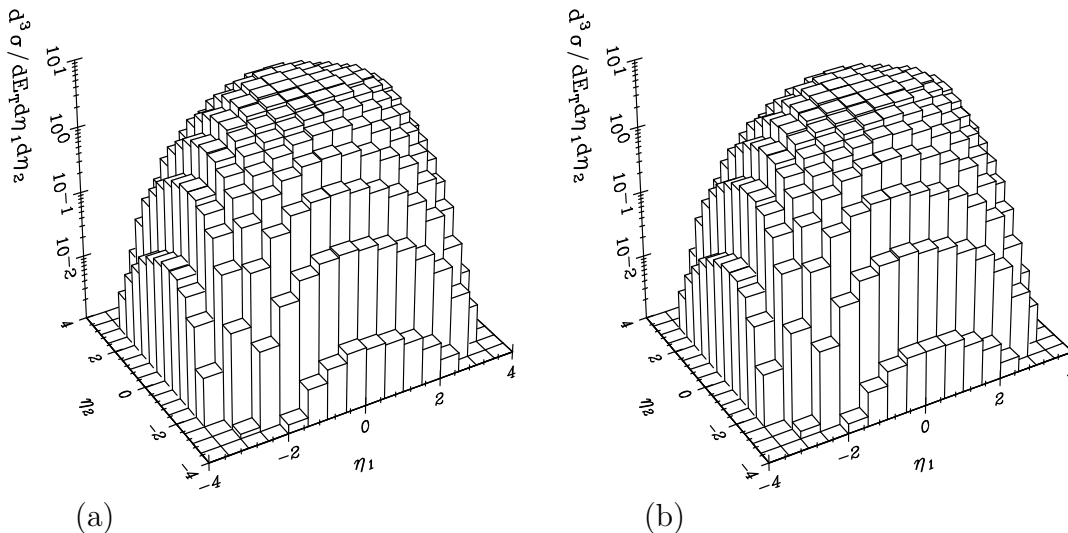


Figure 7: The next-to-leading order triple differential distribution for $45 \text{ GeV} < E_T < 55 \text{ GeV}$ and $\mu = E_{T1}$ for (a) MRSD_0 and (b) MRSD_- parton densities.

standard ‘Snowmass’ cone algorithm [15] with $\Delta R = 0.7$ and require at least two jets in the event. Furthermore, we note that the assignment of which jet is hardest is not infrared safe, so that we must symmetrize over the hardest and next-hardest jets (in transverse energy). The distributions we shall examine require that the hardest jet lie in a certain ‘trigger’ range; each event will be counted twice if the next-hardest jet also lies in this E_T range. The three-dimensional cross section evaluated at $\mu = E_{T1}$, where E_{T1} is the transverse energy of the hardest jet in the event, is shown in Fig. 7 for $45 \text{ GeV} < E_T < 55 \text{ GeV}$. The extension of the phase space to smaller η_2 is seen clearly, along with the rather sharp cutoff at $|\eta_1| \sim 3.5$.

Although the cross sections for the two parton densities appear similar, the difference between the predictions observed at lowest order is preserved. This is illustrated in Fig. 8, where we show the next-to-leading order prediction for the fractional difference ratio defined in Eq. 8. As at lowest order, the difference varies between +23% at $\eta_1 \sim \eta_2 \sim 0$ and -10% at $\eta_1 \sim \eta_2 \sim -2.5$. We note that the ratio is most negative when $x_1 \sim x_T^2$ and $x_2 \sim 1$. This is the region where the singular behaviour of the MRSD_- parton densities dominate over the less singular MRSD_0 distributions [5].

One indicator of the reliability of perturbation theory is the ratio of next-to-leading order to leading order cross sections². This is shown in Fig. 9 for two slices of the triply differential distribution. First we consider the slice $\eta_1 = 0$ and let η_2 vary. At large $|\eta_2|$, the phase space extends beyond the strict leading-order kinematic limit of $\eta_2 < \cosh^{-1}(1/x_T) = 3.68$. As a

²The normalisation is extremely sensitive to the renormalization scale choice in the leading order cross section.

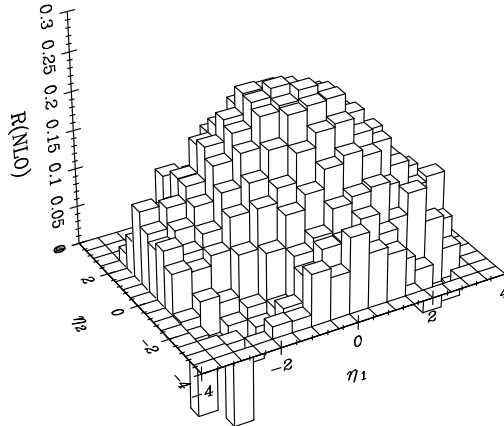


Figure 8: The next-to-leading order prediction for the ratio of the triply differential cross section $R(NLO)$ defined in Eq. 8 for $45 \text{ GeV} < E_T < 55 \text{ GeV}$ and $\mu = E_{T1}$.

consequence, the corrections are large. However, this does *not* signal the emergence of large logarithms which might spoil the applicability of perturbation theory. Rather, the large corrections are due to the more restricted phase space available at leading order, that is the absence of region III of Fig. 1. Towards the edges of available phase space, the leading-order cross section is thus forced artificially to zero, and the ratio goes to infinity. At yet-higher order, however, one expects further corrections to be reasonable (until one approaches the outer edges of region III or its higher-order analogs). Second, we keep $\eta_2 = 0$ fixed and allow η_1 to vary. We see that the corrections for central $|\eta_1|$ are small, however as the magnitude of η_1 approaches the edge of phase space, the next-to-leading order corrections significantly reduce the cross section. In this limit, the second jet is forced to have $E_{T2} \sim E_{T1}$ and the available phase space for soft gluon emission is curtailed. As a consequence, radiative corrections lower the cross section close to the edge of phase space. These corrections are a result of the appearance of large logarithms, and one does expect perturbation theory to behave badly near this edge of phase space. In summary, we see that the triply differential cross section is reliably predicted over the whole range of the $\eta_1 - \eta_2$ plane with the exception of the very large $|\eta_1|$ slices.

We have seen how the shape of the two-dimensional distribution is sensitive to the parton density functions. However, there is also a dependence on the renormalisation and factorisation scales μ_R and μ_F ³ that could in principle obscure the differences due to the structure functions. To get a feeling of how severely the scale uncertainty affects the shape, Fig. 10

³Throughout we choose $\mu_R = \mu_F = \mu$, however, other choices are possible.

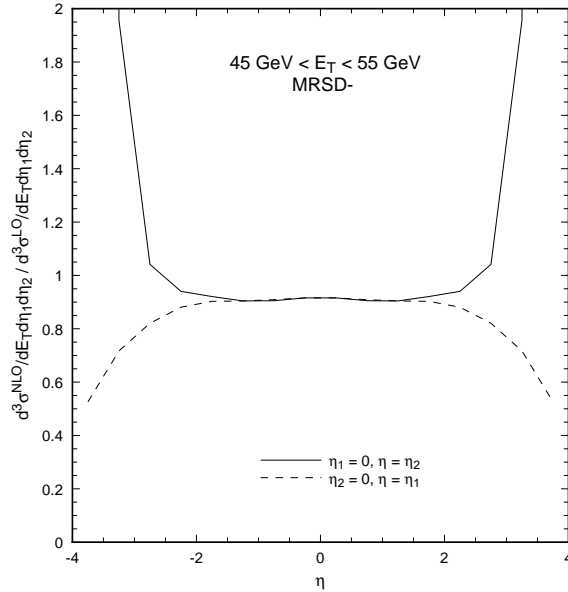


Figure 9: The ratio of next-to-leading order (NLO) to leading order (LO) predictions as a function of η_2 for $\eta_1 = 0$ (solid) and of η_1 for $\eta_2 = 0$ (dashed) for $45 \text{ GeV} < E_T < 55 \text{ GeV}$, $\mu = E_T$ and the MRSD₋ structure functions.

shows the next-to-leading order predictions for the ratio,

$$R = \frac{\int_{E_{T\min}}^{E_{T\max}} dE_T \left(\frac{d^3\sigma}{dE_T d\eta_1 d\eta_2}(\mu = E_{T1}) - c \frac{d^3\sigma}{dE_T d\eta_1 d\eta_2}(\mu = \lambda E_{T1}) \right)}{\int_{E_{T\min}}^{E_{T\max}} dE_T \frac{d^3\sigma}{dE_T d\eta_1 d\eta_2}(\mu = E_{T1})}, \quad (11)$$

for the MRSD₋ parton densities and $\lambda = 0.5$ and 2 . Because the absolute magnitude of the cross section (which depends on $\alpha_s(\mu)$) is poorly predicted, the prediction for $\mu = \lambda E_{T1}$ has been normalised to the cross section for $\mu = E_{T1}$ at $\eta_1 \sim \eta_2 \sim 0$. For $\lambda = 0.5$, $c = 0.93$, while for $\lambda = 2$, $c = 1.08$. We have restricted the pseudorapidity range in the plot to $|\eta_1|, |\eta_2| < 2.5$ since for higher pseudorapidities the next-to-leading order effects are large as discussed above. As a result, for such pseudorapidities, there is a sizeable scale variation. However, for central pseudorapidities, the shape is changed by less than 5% which is significantly less than the difference between the two representative parton distributions.

Once the experimental data are available, it should therefore be possible to extract information on the density of partons in the proton. In addition to the uncertainty in the normalisation of the theoretical predictions, there is a significant uncertainty in the experimental normalisation as well, due to uncertainties in the luminosity measurement, jet energy calibration, jet trigger efficiency, and other aspects⁴. It therefore makes sense to allow the overall normalisation of the theoretical prediction, σ^{TH} , to float, so that by varying c the χ^2

⁴Part of the experimental uncertainty can be eliminated by normalising with respect to the W cross section.

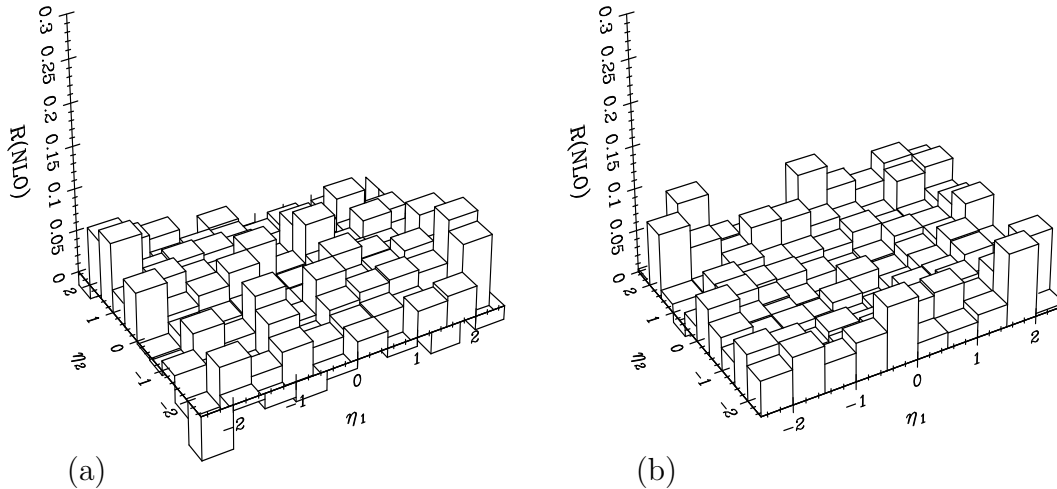


Figure 10: The next-to-leading order prediction for the ratio of the triply differential cross section $R(NLO)$ as defined in Eq. 11 with (a) $\lambda = 0.5$ and (b) $\lambda = 2$ for $45 \text{ GeV} < E_T < 55 \text{ GeV}$ and $\mu = E_{T1}$.

for

$$\int_{E_{T\min}}^{E_{T\max}} dE_T \left(\frac{d^3\sigma^{EXP}}{dE_T d\eta_1 d\eta_2} - c \frac{d^3\sigma^{TH}}{dE_T d\eta_1 d\eta_2} \right), \quad (12)$$

summed over the different η_1, η_2 cells is minimised for a given parameterisation of the parton densities. Finally, the input parameterisations can be adjusted so that the χ^2 is further reduced. This can be done simultaneously for different slices in transverse energy. An even more interesting possibility would be to map out the evolution of the parton densities directly by following trajectories of constant (x_1, x_2) in the $\eta_1 - \eta_2$ plane as a function of E_T .

4 The D0 signed distribution

Recently, the D0 collaboration has presented preliminary data [1, 4] for a particular slicing of the triply differential distribution — the so-called signed pseudorapidity distribution. This amounts to taking two strips of the $\eta_1 - \eta_2$ plane for a fixed transverse energy interval and combining them in reverse directions. The pseudorapidity of the leading jet is constrained to lie in the range $|\eta_1|_{\min} < |\eta_1| < |\eta_1|_{\max}$ and the distribution is plotted as a function of

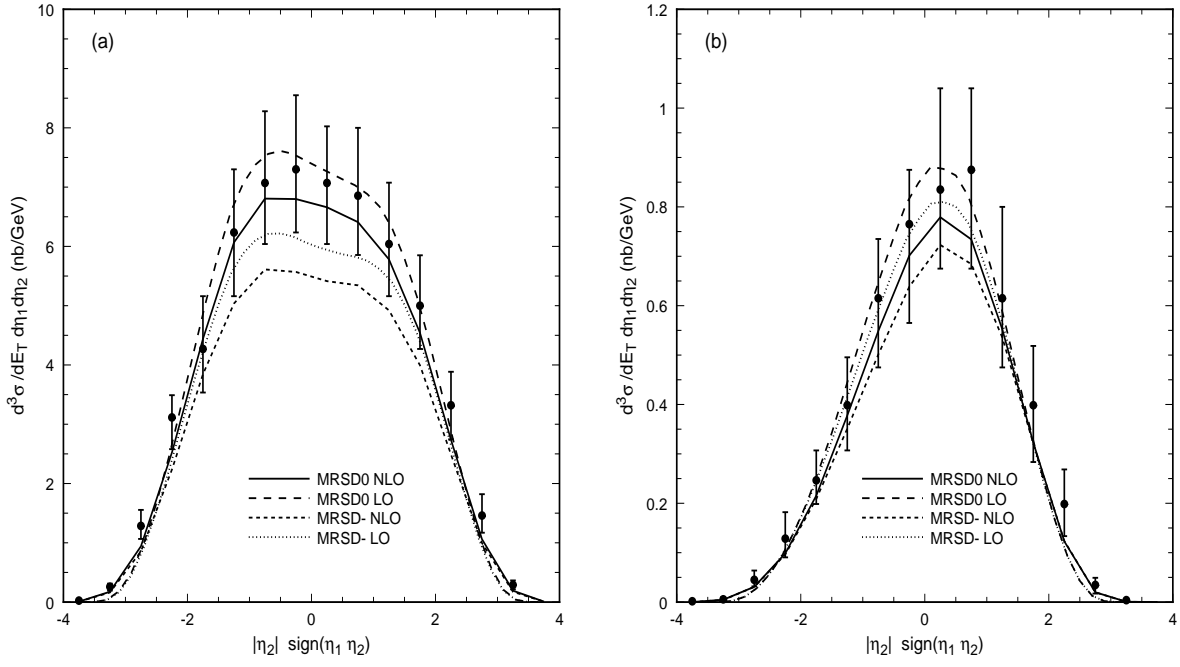


Figure 11: The signed pseudorapidity distribution for (a) $45 \text{ GeV} < E_T < 55 \text{ GeV}$, $0.0 < |\eta_1| < 0.5$ and (b) $55 \text{ GeV} < E_T < 65 \text{ GeV}$, $2.0 < |\eta_1| < 2.5$ at both LO and NLO. The preliminary experimental results from [1] are also shown. The factorisation scale is chosen to be the transverse energy of the hardest jet, $\mu = E_{T1}$.

$$|\eta_2| \text{sign}(\eta_1 \eta_2),$$

$$\frac{d\sigma}{d|\eta_2| \text{sign}(\eta_1 \eta_2)} \equiv \frac{1}{\Delta E_T} \int_{E_{T\min}}^{E_{T\max}} dE_T \frac{1}{2\Delta\eta_1} \left(\int_{|\eta_1|_{\min}}^{|\eta_1|_{\max}} d\eta_1 \frac{d^3\sigma}{dE_T d\eta_1 d\eta_2} - \int_{-|\eta_1|_{\max}}^{-|\eta_1|_{\min}} d\eta_1 \frac{d^3\sigma}{dE_T d\eta_1 d\eta_2} \right), \quad (13)$$

where $\text{sign}(\eta_1 \eta_2) = -1$ if η_1 and η_2 have opposite sign and $+1$ if they have the same sign. Positive values of $|\eta_2| \text{sign}(\eta_1 \eta_2)$ correspond to same-side dijet events, while negative values are associated with opposite-side events. In principle, both strips contain equal information, but combining them serves to reduce the statistical error. Once again, we must sum over the hardest and next-hardest jet in order to ensure that this distribution is infrared-safe.

In the currently available data, D0 has examined two slices in transverse energy, $45 \text{ GeV} < E_T < 55 \text{ GeV}$ and $55 \text{ GeV} < E_T < 65 \text{ GeV}$, and two strips in η_1 , $0.0 < |\eta_1| < 0.5$ and $2.0 < |\eta_1| < 2.5$. As more data become available from the current Tevatron run, this analysis can be extended to cover a larger range of E_T and η .

We first fix η_1 to lie in the central pseudorapidity slice, $0.0 < |\eta_1| < 0.5$ and examine the pseudorapidity of the second jet for the transverse energy interval $45 \text{ GeV} < E_T < 55 \text{ GeV}$. This strip includes the $\eta_1 \sim \eta_2 \sim 0$ region that is sensitive to parton densities at $x \sim 0.05$. We also consider the slice at larger η_1 , $2.0 < |\eta_1| < 2.5$ but for a slightly higher transverse energy interval, $55 \text{ GeV} < E_T < 65 \text{ GeV}$. The predictions for these distributions for both MRSD₀ and MRSD₋ parton densities are shown in Fig. 11 with the preliminary data from the

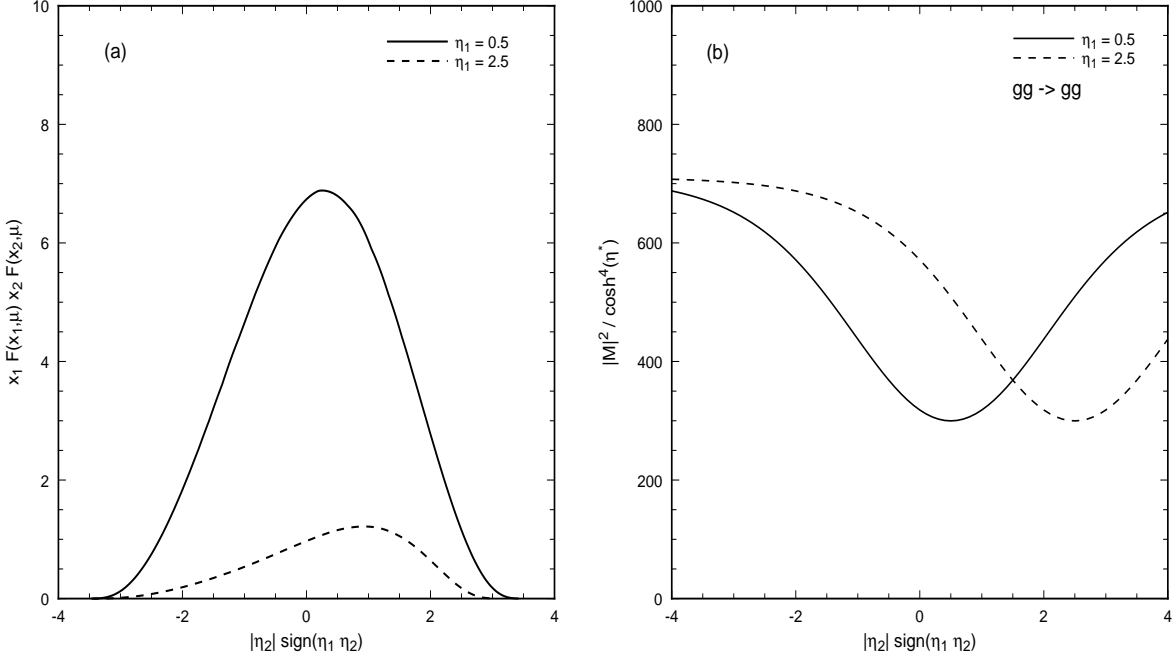


Figure 12: The (a) parton-parton luminosity for the MRSD₋ parton densities and (b) squared matrix elements in the ‘single effective subprocess approximation’ for $\eta_1 = 0.5$ and $E_T = 50$ GeV (solid) and $\eta_1 = 2.5$ and $E_T = 60$ GeV (dashed). The factorisation scale is chosen to be 50 GeV.

D0 collaboration [1]⁵. We see a clear asymmetry favouring smaller values of $|\eta_2| \text{sign}(\eta_1 \eta_2)$. In other words, for $\eta_1 \sim 0$, the opposite-side cross section (negative $|\eta_2| \text{sign}(\eta_1 \eta_2)$) peaks away from $\eta_2 \sim 0$, while the same-side cross section (positive $|\eta_2| \text{sign}(\eta_1 \eta_2)$) monotonically decreases. A similar effect has been observed in the same-side/opposite-side cross section measured by CDF [3].

This is due to an interplay between the parton-parton luminosity and the matrix elements. Fig. 12 shows the parton-parton luminosity in the ‘single effective subprocess approximation’ and the $gg \rightarrow gg$ matrix elements of Eq. 7 as a function of $|\eta_2| \text{sign}(\eta_1 \eta_2)$. We see that the maximum of the parton-parton luminosity occurs at $|\eta_2| \text{sign}(\eta_1 \eta_2) \sim 0.25$ and 0.75 for $\eta_1 = 0.5$ and 2.5 respectively, while the minimum of the matrix elements always lies at $|\eta_2| \text{sign}(\eta_1 \eta_2) = |\eta_1|$. The net effect of the shift in the peak of the parton-parton luminosity to positive $|\eta_2| \text{sign}(\eta_1 \eta_2)$ combined with the shift of the minimum of the matrix elements to larger values of $|\eta_2| \text{sign}(\eta_1 \eta_2)$ is an enhancement of the cross section at negative $|\eta_2| \text{sign}(\eta_1 \eta_2)$ and a depletion at positive $|\eta_2| \text{sign}(\eta_1 \eta_2)$, clearly visible as an asymmetry in Fig. 12.

As suggested by the solid line in Fig. 9, the next-to-leading order corrections reduce the cross section uniformly by about 10% until the kinematic limit on η_2 from the lowest order

⁵We have divided the data by a factor of two to account for the size of the pseudorapidity interval.

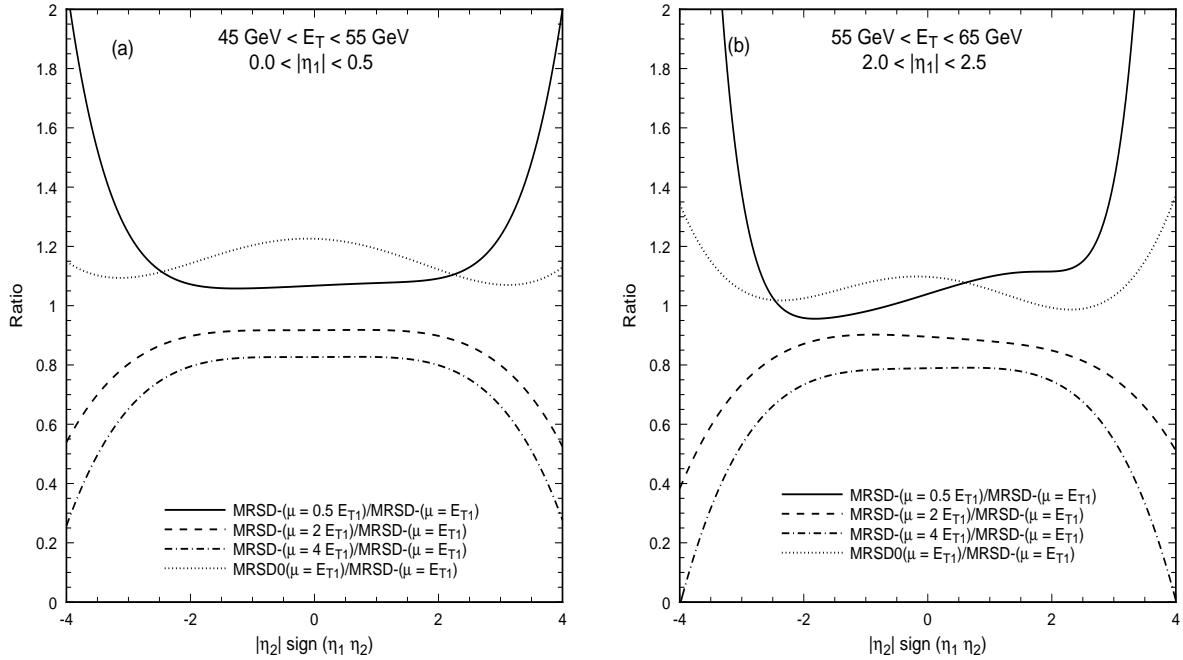


Figure 13: The ratio of next-to-leading order predictions for the signed distribution for the MRSD₋ parton densities evaluated at $\mu = \lambda E_{T1}$ for $\lambda = 0.5$ (solid), $\lambda = 2$ (dashed) and $\lambda = 4$ (dotdashed) relative to that for $\mu = E_{T1}$ for (a) $45 \text{ GeV} < E_T < 55 \text{ GeV}$ and $0.0 < |\eta_1| < 0.5$ and (b) $55 \text{ GeV} < E_T < 65 \text{ GeV}$ and $2.0 < |\eta_1| < 2.5$. The ratio of next-to-leading order predictions for the MRSD₀ and MRSD₋ parton densities with $\mu = E_{T1}$ is shown as a dotted line.

process is approached. We also see that the difference between the MRSD₀ and MRSD₋ predictions is about 23% at $|\eta_2| \sim 0$ as expected from Fig. 8.

At larger pseudorapidities, the next-to-leading order predictions give a much better description of the data than at leading order. The preliminary data appear to favour the MRSD₀ parameterisation at the x values probed here, $x \sim 0.05$. However, the errors are still large, and as mentioned at the end of section 3, there are significant uncertainties in the overall normalisation of the experimental data.

As discussed in the previous sections, there is also an uncertainty in the normalisation of the theoretical cross section due to the choice of renormalisation and factorisation scales. This is particularly evident for the signed distribution since the lowest order cross section is proportional to $\alpha_s^2(\mu_R)$. Even at next-to-leading order, the overall normalisation is still uncertain. However, one would expect that the shape of the distribution is relatively insensitive to varying μ_R . This is illustrated in Fig. 13, which shows the ratio of next-to-leading order predictions for different scales relative to the next-to-leading order MRSD₋ prediction for $\mu = E_{T1}$.

As expected, the normalisation of the small $|\eta_2|$ region is quite sensitive to the choice of scale, however, the *shape* of the distribution for small $|\eta_2|$ is essentially unchanged for the

central η_1 slice, $0.0 < |\eta_1| < 0.5$. For large pseudorapidities, $|\eta_2| > 3$, there is of course a large scale dependence. This is a consequence of exceeding the lowest-order kinematic limit on η_2 ; in this region, an $\mathcal{O}(\alpha_s^3)$ calculation such as the one performed here is in fact a *leading-order* one. As a contrast, the ratio of the next-to-leading order predictions for the MRSD₀ and MRSD₋ parton densities at $\mu = E_{T1}$ are also shown. In addition to a sizeable change in the normalisation, the shape of the distribution around $|\eta_2| \sim 0$ is also changed. It remains an experimental question as to whether this difference in shape can be detected.

5 The CDF same-side over opposite-side ratio

The interpretation of D0 signed distribution measurement hinges strongly on the absolute normalisation of the cross section. Thus one would need to know the jet energy correction well before one can constrain the parton density functions. To circumvent this problem the CDF collaboration has considered a ratio, that of same-side (SS) to opposite-side (OS) cross sections [3]. For the same-side cross section, both jets have roughly the same pseudorapidity, while in the opposite-side cross section the jets are required to have roughly equal, but opposite pseudorapidities. One then forms this ratio, as a function of the pseudorapidity in several transverse-energy slices. In a realistic experimental analysis, the pseudorapidities and transverse energies will be binned so that,

$$\sigma_{SS}(\eta) \Big|_{E_{T\min} < E_T < E_{T\max}} = \int_{\eta-\Delta\eta}^{\eta+\Delta\eta} d\eta_1 \int_{\eta-\Delta\eta}^{\eta+\Delta\eta} d\eta_2 \int_{E_{T\min}}^{E_{T\max}} dE_T \frac{d^3\sigma}{dE_T d\eta_1 d\eta_2}, \quad (14)$$

$$\sigma_{OS}(\eta) \Big|_{E_{T\min} < E_T < E_{T\max}} = \int_{\eta-\Delta\eta}^{\eta+\Delta\eta} d\eta_1 \int_{-\eta-\Delta\eta}^{-\eta+\Delta\eta} d\eta_2 \int_{E_{T\min}}^{E_{T\max}} dE_T \frac{d^3\sigma}{dE_T d\eta_1 d\eta_2}. \quad (15)$$

From these cross sections we form the SS/OS ratio,

$$R_{SS/OS}(\eta) \Big|_{E_{T\min} < E_T < E_{T\max}} = \frac{\sigma_{SS}(\eta) \Big|_{E_{T\min} < E_T < E_{T\max}}}{\sigma_{OS}(\eta) \Big|_{E_{T\min} < E_T < E_{T\max}}}, \quad (16)$$

with the advantage that a large part of the experimental and theoretical uncertainties cancel. However, most of the dependence on the parton densities in the central region where $\eta_1 \sim \eta_2 \sim 0$ is also removed. As we saw in the previous sections, this is exactly the region where there can be a strong dependence on the parton density functions. Nevertheless, we can still study the behaviour of the gluon density at small x by examining the SS/OS ratio at large pseudorapidity. Since the x values probed are much smaller than in the signed pseudorapidity distribution, typically $x \sim 4E_T^2/s$ rather than $x \sim 2E_T/\sqrt{s}$, studying this ratio is to a large extent complementary to studying the D0 signed pseudorapidity distribution.

In the preliminary CDF measurement [3], the jet transverse energy was chosen to lie in four separate bins, $27 \text{ GeV} < E_T < 60 \text{ GeV}$, $60 \text{ GeV} < E_T < 80 \text{ GeV}$, $80 \text{ GeV} < E_T < 110 \text{ GeV}$ and $110 \text{ GeV} < E_T < 350 \text{ GeV}$ and the pseudorapidity interval to be $\Delta\eta = 0.2$.

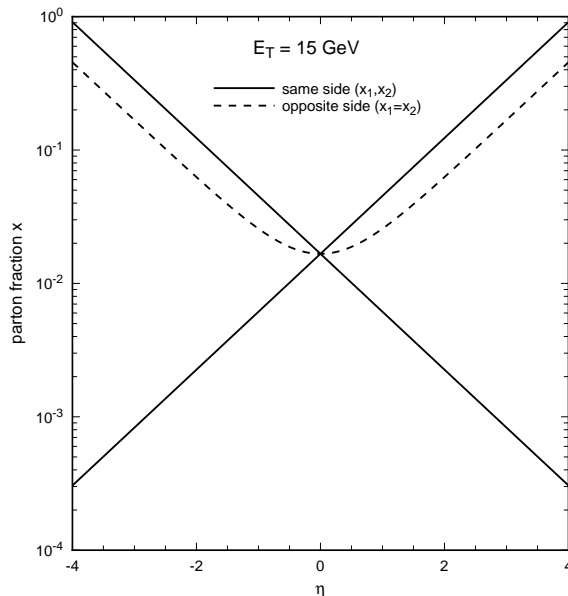


Figure 14: The leading order parton fractions probed by the SS/OS cross section ratio for $E_T = 15$ GeV.

It may prove possible to extend the analysis to smaller transverse energy and include a fifth bin, $15 \text{ GeV} < E_T < 27 \text{ GeV}$. As for the triply-differential and signed rapidity distributions, we must symmetrize explicitly over the leading and next-to-leading transverse energy jets in order to ensure that the sided cross sections are infrared safe. In addition, in order to suppress events with three or more hard jets, an azimuthal angle cut between the two leading jets of $\pi - 0.7 < \Delta\phi < \pi + 0.7$ is applied.

To get a feeling for the range of parton fractions probed by this particular cross section, Fig. 14 shows the three different momentum fractions (using the leading order definition of Eq. 1) as a function of the pseudorapidity for the smallest accessible jet transverse energy $E_T = 15$ GeV. We see that it is possible to probe parton fractions for x values as small as $3 \times 10^{-4} < x < 1$.

The next-to-leading order predictions for the SS/OS ratio for the very low transverse energy bin, $15 \text{ GeV} < E_T < 27 \text{ GeV}$, are shown in Fig. 15. Because very low x values are encountered, the different parton density functions give a broad range of predictions. At present, no data are available for this particular transverse energy range. However, even with relatively large experimental uncertainties one can still easily discriminate between different parton densities. This makes the very small E_T bin particularly interesting.

The region around $\eta = 3$ has the largest sensitivity to different parton density functions, corresponding to a smallest parton fraction of 8×10^{-4} . At larger pseudorapidities (and therefore smaller x values) there is a severe phase space suppression and the cross section (and event rate) decreases rapidly.

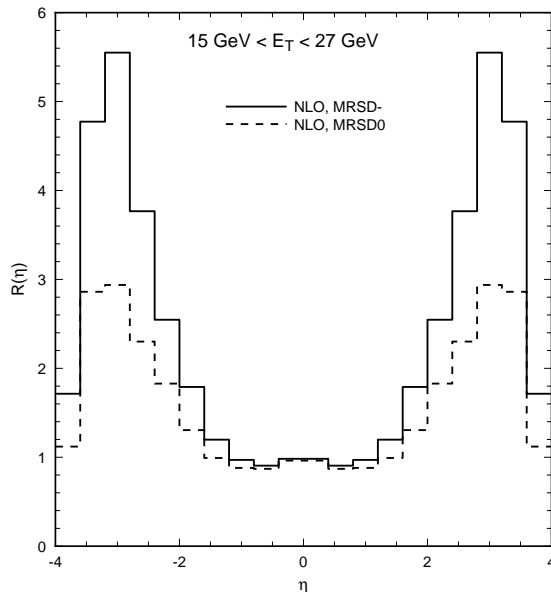


Figure 15: The next-to-leading order predictions for the SS/OS ratio evaluated at $\mu = E_{T1}$ for the MRSD₋ (solid), MRSD₀ (dotted) and MRSA (dashed) parton distributions as a function of η for the smallest E_T bin accessible to the CDF collaboration, $15 \text{ GeV} < E_T < 27 \text{ GeV}$.

In the other four transverse energy bins, the CDF collaboration has published preliminary data which we display along with next-to-leading order predictions for three different parton density sets in Fig. 16. Because the experimental results are preliminary, we should be careful in drawing conclusions from these results for the time being. These results do however prefigure discriminatory powers which should emerge as the experimental errors shrink with the inclusion of more data from the current Tevatron run. Even with the current uncertainties, the smallest E_T bin suggests a deficiency in the density of MRSD₀ partons round $x \sim 10^{-3}$, and in contrast to the signed rapidity distribution discussed in section 4, favors the MRSD₋ set of structure functions.

For the higher transverse energy bins higher x values are sampled and there is not much difference between the different parton density functions. As an example, the highest transverse energy bin is mostly sensitive to parton momentum fractions around 0.1, where the parton density functions are, in principle, tightly constrained. Of course, one should still compare the data with theory. That different parton densities give the same results does not guarantee they are correct; it merely indicates that they either use the same data as a constraint or use the same assumptions to derive the individual parton densities.

For this distribution as well, we should also consider the uncertainty in the theoretical predictions arising from renormalisation and factorisation scale dependence present in perturbative QCD calculations. To study this, Fig. 17 shows the SS/OS ratio for the $27 \text{ GeV} < E_T < 60 \text{ GeV}$ transverse energy bin at pseudorapidity $\eta = 2.6$ as a function of

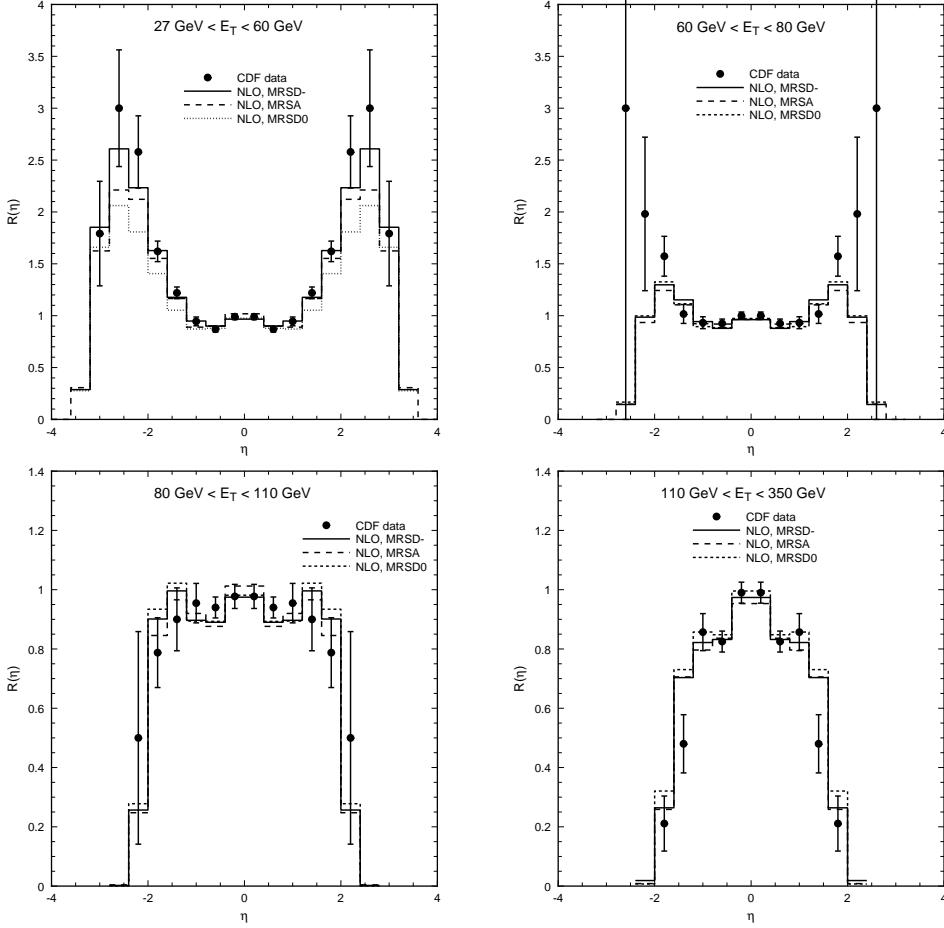


Figure 16: The next-to-leading order (NLO) predictions for the SS/OS ratio evaluated at $\mu = E_{T1}$ for the MRSD₋ (solid), MRSD₀ (dotted) and MRSA (dashed) parton distributions as a function of η for the four transverse energy bins, $27 \text{ GeV} < E_T < 60 \text{ GeV}$, $60 \text{ GeV} < E_T < 80 \text{ GeV}$, $80 \text{ GeV} < E_T < 110 \text{ GeV}$ and $110 \text{ GeV} < E_T < 350 \text{ GeV}$. Also shown is the preliminary CDF data of ref. [3]

$\mu = \mu_R = \mu_F$. This phase space point offers the highest discriminatory power with the currently available data. As an illustration we have chosen the MRSD₋ set which seems to be favoured by these data. The reference scale is the transverse energy of the highest E_T jet in the event, $\mu = E_{T1}$, as in the previous sections. The leading-order prediction does not depend on the strong coupling constant. As the SS and OS cross sections probe the parton densities at different momentum fractions x , it does depend on the factorization scale, but this gives rise only to a trivial scale dependence: the SS to OS ratio rises linearly with $\log(\mu/E_{T1})$. At next-to-leading order, the prediction does depend on the coupling constant, and the overall dependence is less trivial. It so happens that the reference scale, $\mu = E_{T1}$, coincides with the minimum in the variation of the ratio with respect to scale. Either increasing or decreasing the scale results in an increase of the SS/OS ratio. Varying the scale by a factor of two around the reference scale, we get a feeling for the theoretical

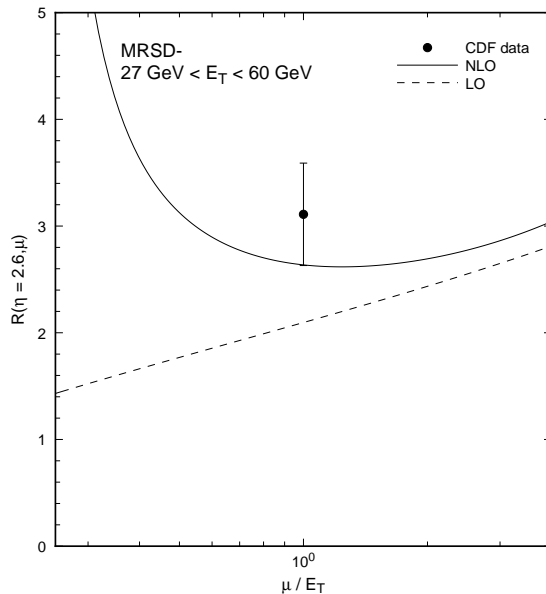


Figure 17: The renormalisation/factorisation scale dependence of the SS/OS ratio for $\eta = 2.6$ in the $27 \text{ GeV} < E_T < 60 \text{ GeV}$ bin using the MRSD₋ structure functions. The data point is taken from ref. [3].

uncertainty. The largest variation comes from reducing μ and increases the cross section by approximately 20%. Due to this uncertainty one cannot really discriminate between the MRSD₋ distributions with $xg(x) \sim x^{-0.5}$ and the more recent MRSA fits with $xg(x) \sim x^{-0.3}$. However, it should be possible to exclude the MRSD₀ distributions once the final CDF data are published. To discriminate between MRSD₋ and MRSA, it will be necessary to make a measurement in the $15 \text{ GeV} < E_T < 27 \text{ GeV}$ transverse energy bin.

Fig. 18 shows the ratio of next-to-leading to leading order predictions (the K -factor) for $27 \text{ GeV} < E_T < 60 \text{ GeV}$ and $80 \text{ GeV} < E_T < 110 \text{ GeV}$ using the MRSD₋ parton densities and $\mu = E_{T1}$. The shape of the SS/OS ratio is basically unchanged between $-2 \leq \eta \leq 2$. For larger pseudorapidities we get a rapid change in the K -factor. This is again mainly due to the fact that the leading order cross section is quickly forced to zero by the kinematic constraints on $2 \rightarrow 2$ scattering, and does *not* indicate the presence of large logarithms which might spoil the applicability of perturbation theory. We have parameterised the K -factor as an even polynomial in η ,

$$K(\eta) = A + B\eta^2 + C\eta^4 + D\eta^6 + E\eta^8. \quad (17)$$

The fitted constants $A \dots E$ for all five transverse energy intervals are given in Table 1. We see that for this double ratio, the corrections are extremely small in the central region.

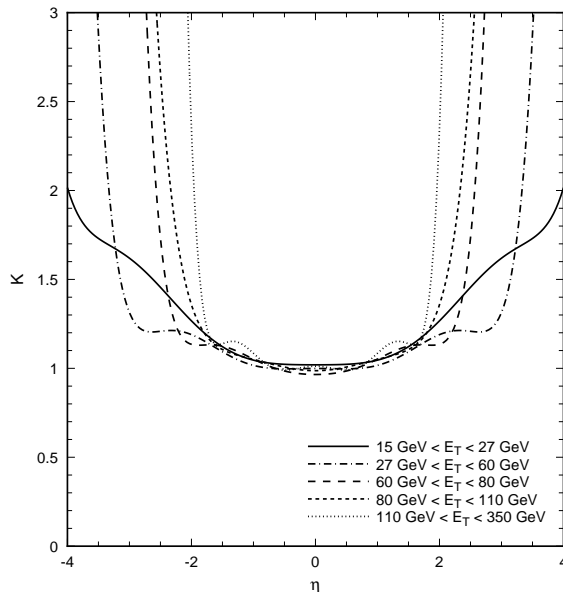


Figure 18: The ratio of next-to-leading to leading order predictions for the SS/OS ratio with $\mu = E_{T1}$ and MRSD₋ parton densities in the five transverse energy intervals.

6 Conclusions

In this paper we have made a detailed study of the two-jet cross section in hadron-hadron collisions for a given range of jet transverse energy as a function of the pseudorapidities of the two jets. This distribution is particularly sensitive to the parton density functions at small ($x \sim \text{few} \times 10^{-3}$) to intermediate ($x \sim \text{few} \times 10^{-2}$) parton momentum fractions for jet transverse energies accessible to the CDF and D0 experiments at Fermilab. For example, parton distributions that are relatively large at small x (and therefore constrained to be relatively small at larger x by the momentum sum rule) lead to a relative enhancement of the same-side two-jet cross section at large pseudorapidities ($\eta_1 \sim \eta_2 \gg 0$) and a relative deple-

Pseudorapidity bin	A	B	C	D	E
15 GeV < E_T < 27 GeV	1.0197	0.0062	0.0226	-0.0025	8.166e-5
27 GeV < E_T < 60 GeV	0.9992	-0.019	0.0453	-0.0094	5.592e-4
60 GeV < E_T < 80 GeV	0.9653	0.072	0.0326	-0.0208	0.0027
80 GeV < E_T < 110 GeV	0.9869	0.0891	-0.0332	0.0057	6.427e-4
110 GeV < E_T < 350 GeV	1.0121	-0.1974	0.4985	-0.2743	0.0457

Table 1: The parameterisation of the K -factor for MRSD₋ in the 5 transverse energy bins. The fitted formula is $K(\eta) = A + B\eta^2 + C\eta^4 + D\eta^6 + E\eta^8$ and is intended to be used for returning the K -factor for the bin, given the center of the bin (that is $\eta = 0.2, 0.6, 1.0, \dots$)

tion for central jets, $\eta_1 \sim \eta_2 \sim 0$. We have studied the next-to-leading QCD corrections to this distribution in some detail. To discuss the properties of the cross section it is convenient to divide the $\eta_1 - \eta_2$ plane into two regions, the central region where the pseudorapidity of the two jets is less than the lowest order kinematic limit, $|\eta_1|, |\eta_2| < \cosh^{-1}(1/x_T)$ and the forward region where the rapidity of one of the jets approaches or exceeds the lowest order boundary. In the central region,

- i) the next-to-leading order corrections are small and perturbation theory works well.
- ii) the scale uncertainty in the overall normalisation is reduced. Varying μ by a factor of 2 about $\mu = E_{T1}$ changes the next-to-leading order prediction by $\mathcal{O}(8\%)$.
- iii) the scale uncertainty in the shape of the distribution is quite small. For the same variation of μ , the relative bin-to-bin correction is less than $\mathcal{O}(2\%)$ — see Fig. 10.

On the other hand, in the forward region,

- i) the next-to-leading order corrections are important and improve the agreement with experimental data.
- ii) there is a considerable scale uncertainty because the corrections calculated in a ‘next-to-leading’ order program corrections are effectively lowest order.

Because the central pseudorapidity region is both sensitive to the parton densities and stable to higher order corrections, the triply differential distribution offers an excellent chance to gain extra information about the distribution of partons in the proton. The current and future runs of the Tevatron at Fermilab should yield copious quantities of two-jet events and once precise experimental data are available, it should be possible to make a determination of the gluon density at small and intermediate x values. However, in addition to the uncertainty in the normalisation of the theoretical predictions, there is also an uncertainty in the experimental normalisation due to uncertainties in the luminosity measurement, in the jet energy calibration, and other effects. The information on the parton densities lies more in the *shape* than the overall normalisation, and one way of determining the parton densities is to allow the overall normalisation of the theoretical prediction, σ^{TH} , to float, so that by varying c the χ^2 for

$$\int_{E_{T\min}}^{E_{T\max}} dE_T \left(\frac{d^3\sigma^{EXP}}{dE_T d\eta_1 d\eta_2} - c \frac{d^3\sigma^{TH}}{dE_T d\eta_1 d\eta_2} \right),$$

summed over the different η_1, η_2 cells in the central pseudorapidity region is minimised for a given parameterisation of the parton densities. By adjusting the input parameterisations, the χ^2 may be further reduced as the predicted shape becomes closer and closer to that observed in the data. Of course, data can be taken for many slices in transverse energy. This allows the possibility of following the evolution of the parton densities directly by following trajectories of constant (x_1, x_2) in the $\eta_1 - \eta_2$ plane as a function of E_T .

At present only preliminary data are available for particular slices of the $\eta_1 - \eta_2$ plane. The signed distribution (sect. 4) presented by the D0 collaboration is primarily sensitive to intermediate x values. As we may expect from the preceding discussion, the shape is well predicted, but the normalisation is uncertain. Nevertheless, the preliminary data appear to favour the MRSD_0 parameterisations (Fig. 11). On the other hand, the same-side to opposite-side cross section ratio presented by the CDF collaboration probes much smaller x values. Once again, the shape is relatively unchanged by including the next-to-leading order corrections. As shown in Fig. 16, the preliminary data (again with large errors) appear to favour the more singular MRSD_- parameterisation. Of course, with the current experimental data sample, no definitive conclusion can be drawn. However, if these tentative observations are accurate, it would imply that the data favour the parton density with the largest density of gluons at *both* $x \sim \text{few} \times 10^{-3}$ *and* $x \sim \text{few} \times 10^{-2}$. In other words, there are more gluons present in the small and intermediate x regions than expected from the momentum sum rule, which may in turn suggest that the density of gluons is not as well determined by direct photon data (WA70) as previously thought. Data from the current Tevatron run should help to provide an answer to this puzzle.

Acknowledgements

We are happy to acknowledge many stimulating discussions with members of the D0 and CDF collaborations, in particular, Brad Abbott, Jerry Blazey, Teri Geld, Eve Kovacs and Freedy Nang. We also thank Alan Martin for constructive comments. EWNG thanks the Fermilab theory group for its kind hospitality in July and August when this work was initiated.

References

- [1] D0 Collaboration, presented by Harry Weerts, Ninth Topical Workshop on Proton – Anti-proton Collider Physics, Tsukuba, Fermilab preprint, FERMILAB-CONF-94/35-E.
- [2] S. D. Ellis, Z. Kunszt and D. E. Soper, Phys. Rev. Lett. **69**, 1496 (1992).
- [3] CDF Collaboration, F. Abe *et al*, Fermilab preprint, FERMILAB-CONF-93/203-E; CDF Collaboration, presented by Eve Kovacs, Eighth Meeting of the Division of Particles and Fields of the American Physical Society, Albuquerque, New Mexico, August 1994, Fermilab preprint FERMILAB-CONF-94/215-E.
- [4] D0 collaboration, presented by Freedy Nang, Eighth Meeting of the Division of Particles and Fields of the American Physical Society, Albuquerque, New Mexico, August 1994, Fermilab preprint FERMILAB-CONF-94-341-E.
- [5] W. T. Giele, E. W. N. Glover and D. A. Kosower, Phys. Lett. **B339**, 181 (1994).
- [6] B. Combridge and C.J. Maxwell, Nucl. Phys. **B239**, 429 (1984).
- [7] WA70 Collaboration, M. Bonesini *et al*, Z. Phys. **C38**, 371 (1988).
- [8] A. D. Martin, R. G. Roberts and W. J. Stirling, Phys. Lett. **B306**, 145 (1993).
- [9] A. D. Martin, R. G. Roberts and W. J. Stirling, Durham preprint DTP/94/34.
- [10] R. K. Ellis and J. Sexton, Nucl. Phys. **B269**, 445 (1986).
- [11] Z. Bern and D. A. Kosower, Nucl. Phys. **B379**, 451 (1992); Z. Kunszt, A. Signer, and Z. Trocsanyi, Nucl. Phys. **B411**, 397 (1994).
- [12] W. T. Giele, E. W. N. Glover and D. A. Kosower, Phys. Rev. Lett. **73**, 2019 (1994).
- [13] W. T. Giele and E. W. N. Glover, Phys. Rev. **D46**, 1980 (1992).
- [14] W. T. Giele, E. W. N. Glover and D. A. Kosower, Nucl. Phys. **B403**, 633 (1993).
- [15] See, for example, J.E. Huth *et al*, in Research Directions for the Decade, Proceedings of the 1990 Division of Particles and Fields Summer Study, Snowmass, 1990, edited by E.L. Berger (World Scientific, Singapore, 1992), p.134.